Stress–Strain Behavior in Uniaxial Compression of Polymer Gel Beads

Runi D. Egholm,[1] Søren F. Christensen,[2] Peter Szabo[1]

[1]*Department of Chemical Engineering, Danish Polymer Centre, Technical University of Denmark, 2800 Lyngby, Denmark*
[2]*VersaMatrix A/S, Gamle Carlsbergvej 10, 2500 Valby, Denmark*

Received 15 November 2004; accepted 27 June 2005
DOI 10.1002/app.24715
Published online in Wiley InterScience (www.interscience.wiley.com).

ABSTRACT: A method for carrying out mechanical testing on spherical microparticles (Versabeads™) has been evaluated using an incompressible viscoelastic finite element model. The mechanical test is based on the compression of a single bead from which stress–strain data are obtained. Simulations based on the finite element model are used to investigate whether or not an apparent elastic modulus found as the slope of the initial close to linear stress–strain curve can be related to the real elastic modulus. The numerical results indicate that the apparent modulus is in fact related to the elastic shear modulus and that the relation $E_{app} \approx 4G$ can be used to obtain the shear modulus from the mechanical test. These results, however, only apply for purely elastic beads. The finite element solution has also been compared to the Hertz's expression relating axial displacement and compression force. Good agreement with the Hertz's expression is obtained at axial displacements below 10% and fit of the Hertz's expression to simulated force–displacement curves leads to a Hertz's modulus that is equal to $4G$. This is expected for incompressible materials. J Appl Polym Sci 102: 3037–3047, 2006

Key words: compression; computer modeling; gels; mechanical properties; viscoelastic properties

INTRODUCTION

When a highly crosslinked polymer sample (rubber) is strained, the initial stress–strain relationship is usually linear. The proportionality factor, e.g., the elastic modulus, then gives an indication of the rigidity of the sample (see Refs. 1 and 2). To reduce the complexity of defining and measuring the macroscopic stresses and strains, the test samples are prepared in such a way that their geometry is suitable for carrying out simple mechanical tests such as simple shear (cubes) or shear free experiments (elongation of long rods). However, it is not always possible to produce test samples with these geometries. In this work, an experimental method for measuring the mechanical properties of spherical particles is investigated. The particles are polymer gel beads (Versabeads™) that are used in synthesis and purification steps in the pharmaceutical and biochemical industry. The bead particles range from 40 to 700 μm in diameter and their chemical and mechanical properties can be controlled through the preparation conditions.[3,4] The test method is based on uniaxial compression of a single particle placed between two planar surfaces. During the compression, the force and the central lateral expansion are recorded. The purpose of the test is to extract key material properties such as the elastic modulus from the data collected during the test. Similar studies have been carried out previously by Andrei et al.,[5] Knaebel et al.,[6] and Liu et al.[7] for spherical gel particles swollen in water. In these works, the classical theory of Hertz[8] and also the extended theory by Tatara[9] were used on force–displacement data from uniaxial compression of a single particle to investigate material properties such as the elastic modulus and the Poisson's ratio. However, for the experimental method investigated in the present study it is more desirable to obtain the elastic modulus from the measured force and the central lateral expansion of the bead because these data are obtained directly from the test. This requires that a measure of the macroscopic stress and strain can be found using these data and that an elastic modulus is obtainable from the data. The question is whether such an elastic modulus can be related to the real elastic (or Young's) modulus that is necessary if the method is to be used as a reliable means for characterizing the mechanical properties of the beads. Furthermore, depending on the preparation conditions, the elasticity of the beads can be varied within a broad range. Also the presence of viscoelastic effects has to be considered. In the presence of a solvent, the Versabeads™ can take up considerable amounts of solvent (e.g., water) in which case the resultant

Correspondence to: P. Szabo (ps@kt.dtu.dk).
Contract grant sponsor: Danish Technical Research Council; contract grant number: 26-03-0282.

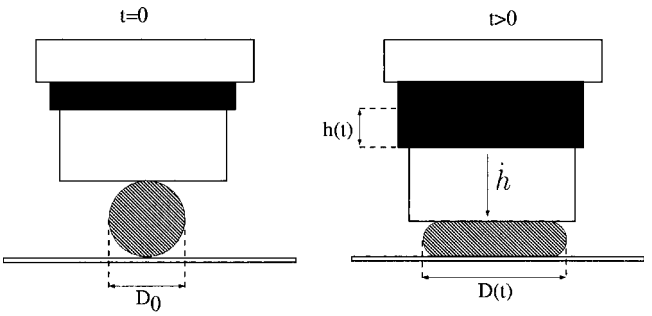

Figure 1 Close up of the bead deformation during the test [cf. Fig. 8)]. $h(t)$ is the axial displacement at time t, $\dot{h}$ is the displacement velocity, $D(t)$ it the central lateral diameter at time t, and D_0 is the initial diameter.

swelling decreases the rigidity of the beads. Therefore, it is also important to investigate to what extent the test is applicable when beads are in a swollen state. To investigate the compression experiment, a viscoelastic finite element model based on the split Lagrangian–Eulerian approach described by Harlen et al.[10] is set up and solved. An alternative technique would be to use the Lagrangian method of Rasmussen.[11,12]

THEORY

In the limit of small axial displacements, the relationship between the compression force F and the axial displacement h for an elastic sphere compressed between two flat smooth surfaces was solved by Hertz in 1882.[8] He derived the expression given in eq. (1).

$$F = \left[\frac{4}{3}\sqrt{R_0}E^*\right]\left(\frac{h}{2}\right)^{3/2} \tag{1}$$

In eq. (1), h is the displacement (cf. Fig. 1), R_0 is the initial radius, F is the measured force, and E^* is the Hertz's modulus that is related to Young's modulus by

$$E^* = \frac{E}{1-\nu^2}$$

Here ν is Poisson's ratio equal to 0.5 for incompressible materials. The Hertz's expression is only valid for displacements up to about 10% and furthermore it is only valid for purely elastic materials.

To use eq. (1) to obtain the modulus the axial displacement h must be known. However, we are interested in investigating whether there is a relationship between the force and the central lateral expansion D (cf. Fig. 1) and whether such a relationship can be used to obtain the elastic modulus. We therefore define the apparent macroscopic strain $\gamma(t)$ as

$$\gamma(t) = \frac{D(t) - D_0}{D_0} \tag{2}$$

Here D_0 is the initial diameter of the bead. The apparent macroscopic stress $\sigma(t)$ is then defined as the ratio between the compressive force, $F(t)$, and the central lateral cross-sectional area, i.e.

$$\sigma(t) = \frac{F(t)}{\frac{\pi}{4}[D(t)]^2} \tag{3}$$

When the stress σ is depicted as a function of the strain γ using real measurement data, the curves generally have the form sketched in Figure 2. As shown in the figure, the initial part of the curve is close to linear and therefore we define an apparent modulus E_a as the slope of the initial part of the curve. To investigate whether this apparent modulus is related to the real elastic modulus, a finite element model is implemented and solved. The results from this model are then used to compare the model input modulus to the apparent modulus obtained from simulated data.

Although the Hertz's expression cannot be used on our experimental data it can be used for verification of force–displacement data obtained from our finite element model in the elastic limit.

Mathematical model

We now turn to the mathematical model used to model the deformation. Here the notion of Bird et al.[13] is used. The beads are practically perfect spheres and therefore the geometry to be modeled has axial and radial symmetry. This means that only a quarter of the cross section of a sphere needs to be considered, cf. Figure 3. As time proceeds the axial compression results in a radial expansion of the

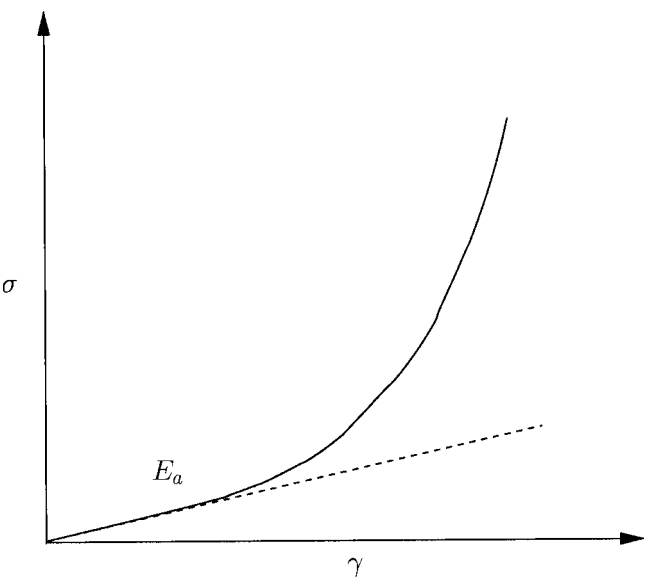

Figure 2 Sketch of a stress–strain curve and how E_a is found.

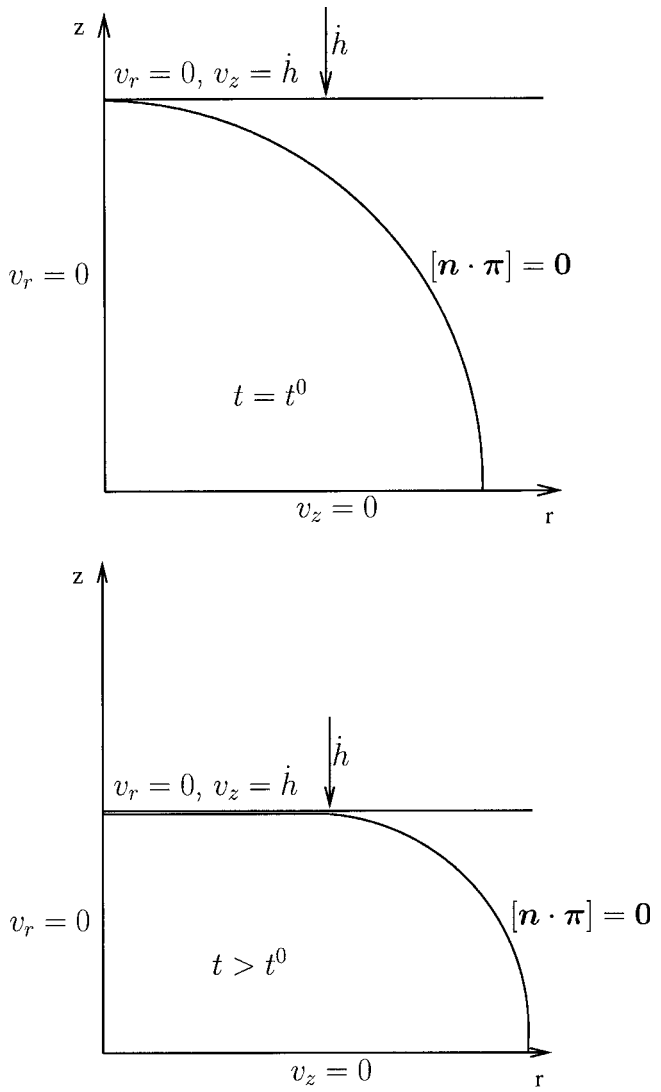

Figure 3 Sketch of the geometry at $t = t^0$ and $t > t^0$. BCs are also shown.

sphere. Locally, the position of each material point can be calculated using displacement functions having the form

$$r = r(r^0, z^0, t^0, t) \quad z = z(r^0, z^0, t^0, t)$$

where r^0 and z^0 are initial positions at time t^0. However, because we have chosen to solve the model using a split Eulerian–Lagrangian method,[10] the positions are found from velocities by linear extrapolation:

$$r = r' + v_r \Delta t \quad z = z' + v_z \Delta t$$

where Δt is the time step and r' and z' are positions from the previous time step. The stresses are split into a purely viscous part T^v and a purely elastic part T^e. The Mooney-Rivlin constitutive equation is used for the elastic part that leads to the stress tensor given in eq. (4).[14]

$$\tau = \tau^v + \tau^e = -\mu\dot{\gamma} + G[(1-q)\gamma_{[0]} + q\gamma^{[0]}] \tag{4}$$

In eq. (4), $\dot{\gamma}$ is the rate of strain tensor, $\gamma_{[0]}$ is the upper convected relative strain tensor, $\gamma^{[0]}$ is the lower convected relative strain tensor, μ is the viscosity, and G is the shear modulus. The parameter q determines the relative contribution to the elastic stress from each of the strain tensors. If $q = 0$, the elastic contribution reduces to that of the Neohookean case. It is also noted that for small strains, the Mooney-Rivlin equation reduces to the constitutive equation for a Hookean spring because both relative strain tensors tend toward the infinitesimal strain tensor $\gamma = \nabla u + (\nabla u)^T$ in the limit of small displacement gradients (u is the position of a material point relative to the initial position).[13]

Conservation of momentum is written in terms of the equation of motion with inertia and gravity neglected leading to

$$0 = [\nabla \cdot \pi] = [\nabla \cdot (p\delta + \tau)] \tag{5}$$

In eq. (5), δ is the unit tensor and π is the total stress tensor. We assume that the beads are incompressible and thus the equation of continuity is satisfied, i.e.

$$0 = \nabla \cdot v \tag{6}$$

To complete the model the boundary conditions (BCs) are identified. In Figure 3(a) a sketch of the initial undistorted geometry and the BCs can be seen. It is noted that at the interface between the sphere and the platen the no slip BC is applied, i.e., $v_r = 0$. Furthermore, it is assumed that pressures and stresses balance at the free surface, which in the case of negligible surface tension can be written as

$$[n \cdot \pi] = P_a n \tag{7}$$

where n is the outward directed normal vector on the surface and P_a corresponds to the external pressure. Because the pressure is determined up to the addition of a constant, we choose the external pressure to be $P_a = 0$. This ''natural'' BC is used directly in the finite element formulation of the problem.

Finite element formulation

The model is rewritten into its finite element formulation (or weak formulation) by first multiplying the equation of motion and the continuity equation with a trial function ϕ and integrating over the sphere volume (Ω). This leads to eqs. (8) and (9).

$$0 = \int_\Omega \phi[\nabla \cdot \pi]\, d\Omega \tag{8}$$

$$0 = \int_\Omega \phi(\nabla \cdot v)\, d\Omega \tag{9}$$

Because of axial symmetry, there is no θ-dependence for any of the variables. This means that the differential volume $d\Omega$ can be replaced by the differential surface $dS = r\, dr\, dz$. Equation 8 may be rewritten by integrating by parts the highest order terms and using the Gauss–Ostrogradskii divergence theorem. This leads to eq. (10) that, for clarity, is written out into its components.

$$\begin{aligned} 0 = &\int_{\partial S} \phi[\delta_r(\pi_{rr}n_r + \pi_{zr}n_z) + \delta_z(\pi_{rz}n_r + \pi_{zz}n_z)]r\, dr\, dz \\ &- \int_S \delta_r\left(\frac{\partial\phi}{\partial r}\pi_{rr}r + \frac{\partial\phi}{\partial z}\pi_{zr}r + \phi\pi_{\theta\theta}\right) \\ &+ \delta_z\left(\frac{\partial\phi}{\partial r}\pi_{rz}r + \frac{\partial\phi}{\partial z}\pi_{zz}r\right) dr\, dz \end{aligned} \tag{10}$$

In eq. (10), δ_r and δ_z are the unit vectors in the r and z direction, n_r and n_z are the components of the outward directed normal vector on the free surface, and ∂S corresponds to the free surface in the (r, z) plane. From the natural BC stated earlier, it is clear that the surface integral in 10 is zero (cf eq. (11)).

$$\delta_r(\pi_{rr}n_r + \pi_{zr}n_z) + \delta_z(\pi_{rz}n_r + \pi_{zz}n_z) = [n \cdot \pi] = 0 \tag{11}$$

However, to solve the model it is still necessary to specify the pressure (equal to 0) on the surface. The finite element formulation of the model is thus given by eqs. (9) and (10) with the surface integral in eq. (10) being zero.

Discretization

We have chosen to discretize the domain using triangular elements partly because of prior experience with the triangular elements[10] and because triangles are well suited for filling up the computational domain under consideration, cf. Figure 3. Isoparametric quadratic triangular elements are used for the velocities and positions and isoparametric linear triangles are used for the pressures. This is a stable method for Stokes flow problems.[15] The variables are discretized locally on each element using local interpolation functions as shown in eq. (12).

$$\begin{aligned} v_r = \sum_{i=1}^{6} N_i \hat{v}_{r,i} \quad v_z = \sum_{i=1}^{6} N_i \hat{v}_{z,i} \quad p = \sum_{i=1}^{3} L_i \hat{p}_i \\ z = \sum_{i=1}^{6} N_i \hat{z}_i \quad r = \sum_{i=1}^{6} N_i \hat{r}_i \end{aligned} \tag{12}$$

In eq. (12), N_i is the value of the local quadratic interpolation functions used for interpolating velocities and positions at local node i, whereas L_i is the value of the linear interpolation functions at local node i used for interpolating the pressure. The variables with hats correspond to nodal values where the nodes in an element can be seen in Figure 4.[15] The (arbitrary) trial functions ϕ are chosen to be the quadratic interpolation functions for the momentum balance and the linear interpolation function for the equation of continuity.

The terms that enter the relative strain tensors consist of the displacement gradients that can be calculated explicitly from the (known) nodal positions ($\hat{r}$) and the local interpolation functions. The rr-component of the relative strain tensor $\gamma_{[0]}$ is discretized as

$$\begin{aligned} \gamma_{[0],rr} &= 1 - \left[\left(\frac{\partial r}{\partial r^0}\right)^2 + \left(\frac{\partial r}{\partial z^0}\right)^2\right] \\ &\simeq 1 - \left[\left(\sum_{i=1}^{6} \frac{\partial N_i}{\partial r^0}\hat{r}_i\right)^2 + \left(\sum_{i=1}^{6} \frac{\partial N_i}{\partial z^0}\hat{r}_i\right)^2\right] \end{aligned}$$

and similarly for the other components of $\gamma_{[0]}$. This means that all contributions from the elastic stresses can be moved to the RHS of the equation system. However, we have experienced that this results in a quite unstable system when elastic stresses are large relative to the viscous contribution.

We believe that the explicit calculation of the elastic stresses results in an ill-conditioned system when the elastic stresses are large compared to the viscous stresses. Therefore, some of the elastic terms from

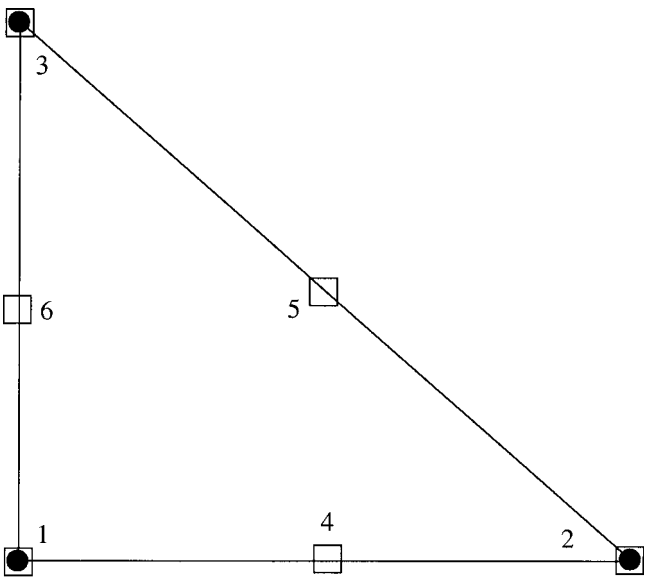

Figure 4 Triangular element. ● linear (pressure) nodes; □ quadratic (velocity) nodes. Numbers indicate local node numbering.

$\gamma_{[0]}$ are split up using linear interpolation of positions in time, e.g.

$$\left(\frac{\partial r}{\partial r^0}\right)^2 \simeq \left(\frac{\partial r}{\partial r^0}\right)\left(\frac{\partial r'}{\partial r^0} + \Delta t\ \frac{\partial v_r}{\partial r^0}\right)$$
$$\simeq \left(\sum_{i=1}^{6}\frac{\partial N_i}{\partial r^0}\hat{r}_i\right)\left(\sum_{i=1}^{6}\frac{\partial N_i}{\partial r^0}\hat{r}'_i + \Delta t\sum_{i=1}^{6}\frac{\partial N_i}{\partial r^0}\hat{v}r_i\right)$$

Hence, these elastic terms now contain both implicit and explicit parts. Because the terms in $\gamma^{[0]}$ are gradients of the initial positions (e.g., $\partial r^0/\partial r$), these are not split up and are just calculated explicitly. This, however, results in an increasingly unstable system as q increases ($0 \leq q \leq 1$).

After introducing discretized variables, the full system is set up by calculating the integrals numerically and summing the contributions from each node. This leads to a system of $2N_v + N_p$ equations with $2N_v + N_p$ unknowns (i.e., nodal velocities and pressures). Here, N_v is the total number of velocity nodes and N_p is the total number of pressure nodes. Integration of the discretized finite element equations is carried out numerically by transforming the global coordinates into local coordinates as explained in, e.g., Ref. 15.

Numerical procedure

The system of equations is solved for the nodal velocities and pressures and then a step forward in time is carried out by using the nodal velocities, i.e.

$$r_i^{\text{new}} = r_i + v_{r,i}\Delta t$$
$$z_i^{\text{new}} = z_i + v_{z,i}\Delta t$$

Here, r_i and z_i are nodal (i) positions used in the last calculation of velocities and positions and Δt is the time step that needs to be relatively small so as to avoid large errors accumulated from the first-order time stepping procedure.

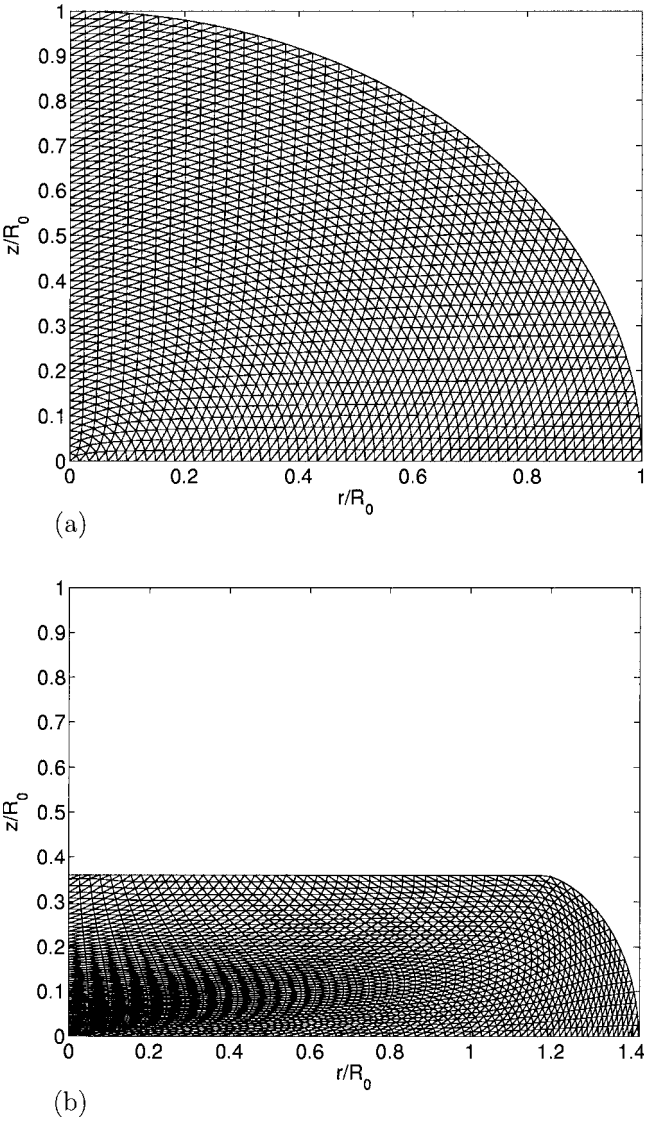

Figure 5 Mesh with 3719 elements, 7620 velocity nodes, and 1951 pressure nodes. (a) Geometry before start of simulation; (b) distorted geometry after simulation to 65% axial displacement.

Convergence analysis

The convergence of the finite element scheme is investigated for the velocities, pressure, and compression force. Since no analytical solution exists for the sphere geometry, the analysis is based on a reference solution obtained on a fine mesh with 3719 elements, cf. Figure 5. To compare solutions obtained on coarser meshes with the reference solution, the solution on the fine mesh is interpolated onto the coarser meshes (with cubic spline interpolation). The parameters used were chosen such that the dimensionless number Λ defined in Results and Discussion Section was $\Lambda = 10^2$. Furthermore $q = 0.1$ was used in the analysis and the solution on the various meshes was compared at 20% compression. In Figure 6 the error in the velocities can be seen. The error is calculated as the 2-norm of the difference between the interpolated reference solution and the actual solution on each mesh normalized by the number of nodes, i.e.

$$\text{error} = \frac{1}{N_{\text{nodes}}}\frac{\|v_{\text{ref}} - v\|_2}{\|v_{\text{ref}}\|_2} \tag{13}$$

From Figure 6, it is seen that third-order convergence is obtained for the velocities. This is in agreement with the expected order of convergence that is $O(h^{p+1})$ where p is the interpolation order in the finite element scheme.[15] In Figure 7 the error in the

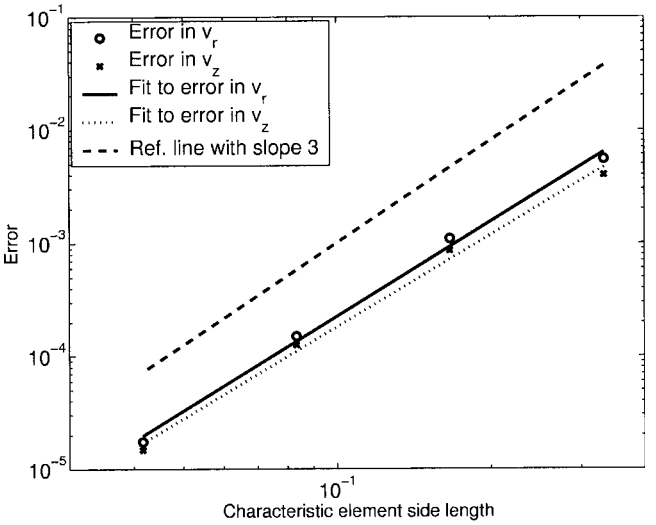

Figure 6 Convergence analysis. 2-norm of the error in the velocities versus a characteristic element side length. The error is relative to a reference solution obtained on a fine mesh (3719 elements). The slope for the error in v_r is 2.78 and the slope for the error in v_z is 2.70. For comparison a reference line with a slope of 3 is also shown.

pressure and the compression force can be seen. As expected we obtain second-order convergence for the pressure. Furthermore second-order convergence is seen for the forces because both the pressure and the velocities enter the calculation of the forces (see next section) and the convergence is controlled by the variable with the lowest convergence order. Hence, the convergence analysis shows that the expected convergence is obtained for all variables.

Calculation of the compression force

To calculate the compression force, we have implemented a method described by Rasmussen and Hassager.[16] This method uses the discretized finite element equations to calculate the force.

It is noted that the force in axial direction at $z = h$ by definition is given by

$$F = \int_{A_c} \pi_{zz}|_{z=h}\, dS = 2\pi \int_{\Gamma_c} \pi_{zz}|_{z=h}\, r\, dr\, dz \qquad (14)$$

Here, A_c is the part of the surface in contact with the moving platen and Γ_c is the corresponding part of the surface in the (r, z) plane. If ϕ_i, $l \in [1,\ldots,L]$ denote the trial functions associated with nodes on the contact interface then the sum of all ϕ_l equals one, i.e., $\Sigma_{l=1}^{L}\, \phi_l = 1$. We may therefore rewrite eq. (14) as

$$F = 2\pi \sum_{l=1}^{L} \int_{\Gamma_c} \phi_l \pi_{zz} r\, dr\, dz \qquad (15)$$

From eq. (10) it is seen that

$$\int_{\partial S} \phi(\pi_{rz} n_r + \pi_{zz} n_z) r\, dr\, dz = \int_S \left(\frac{\partial \phi}{\partial r}\pi_{rz} + \frac{\partial \phi}{\partial z}\pi_{zz}\right) r\, dr\, dz \qquad (16)$$

The contact surface between the sphere and the moving platen is horizontal, thus at $z = h$, $n_r = 0$, and $n_z = 1$. Furthermore, no shear stresses exist on the contact interface because of the no slip BC. Hence, from eq. (16) it follows that

$$\sum_{l=1}^{L} \int_{\Gamma_c} \phi_l \pi_{zz} r\, dr\, dz = \sum_{l=1}^{L} \int_{S_c} \frac{\partial \phi_l}{\partial z} \pi_{zz} r\, dr\, dz \qquad (17)$$

Here the domain of integration S_c corresponds to the elements adjacent to the contact interface because the trial functions ϕ_l are zero on all other elements. Comparison of eqs. (15) and (17) leads to

$$F = 2\pi \sum_{l=1}^{L} \int_{S_c} \frac{\partial \phi_l}{\partial z} \pi_{zz} r\, dr\, dz = 2\pi \sum_{l=1}^{L} \int_{S_c} \left(\frac{\partial \phi_l}{\partial z} p + \frac{\partial \phi_i}{\partial z} \tau_{zz}\right) r\, dr\, dz \qquad (18)$$

Equation 18 is then used to calculate the force.

EXPERIMENTAL SETUP AND PROCEDURE

Now a short description of the experimental setup and procedure for measuring stress–strain data is

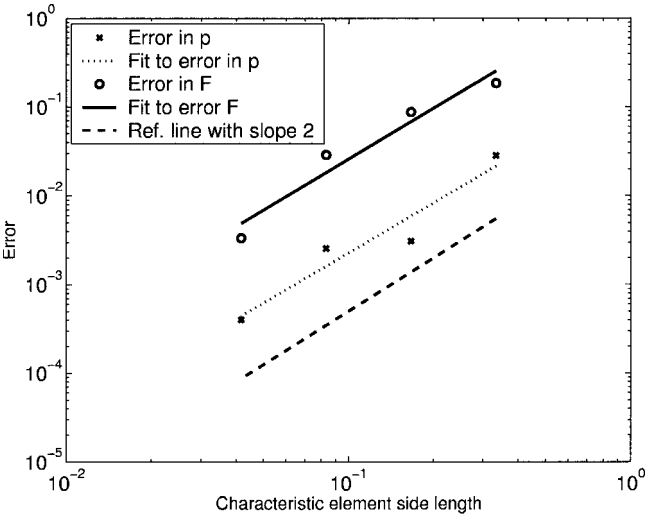

Figure 7 Convergence analysis. 2-norm of the error in the pressure versus a characteristic element side length. Also shown is the error in the compressive force. The error is relative to a reference solution obtained on a fine mesh (3719 elements). The slope for the error in p is 1.87 and the slope for the error in F is 1.90. For comparison a reference line with a slope of 2 is also shown.

given. In Figure 8, a side view sketch of the setup for the compression test can be seen. The bead (A) is placed on a microscope slide (B) and the microscope slide is placed on an inverted microscope (F). Using the image from the microscope, the bead is placed directly under a probe (C) that is connected to a linear DC actuator (D). The compression velocity is thus controlled using the linear actuator. The load applied to the bead during the test is measured using a load cell consisting of a linear strain gauge (E) that has a compliance of about 0.17 μm/m N. As will be clear in later section, the magnitude of the compressive force during a measurement is on the m N scale, wherefore the compliance of the load cell has to be taken into account if one needs to know the compression velocity.

The load cell has a resolution of about 0.1 m N and the central lateral diameter of the bead can be determined with a resolution of about 1 μm. During the test, the image output from the microscope is recorded as a video sequence onto a computer that makes it possible to measure the central lateral expansion as a function of time in the subsequent data handling (cf. Fig. 1).

As mentioned in the introduction section, the beads will swell considerably when immersed into a solvent and in fact the beads will be swollen in all practical applications. Therefore, it is important to know the mechanical properties in the swollen state, which also means that it is necessary to be able to carry out the compression test on single beads in the swollen state. This is carried out by adding a drop of solvent (usually water) on top of a bead and letting it reach its equilibrium degree of swelling before it is placed under the probe.

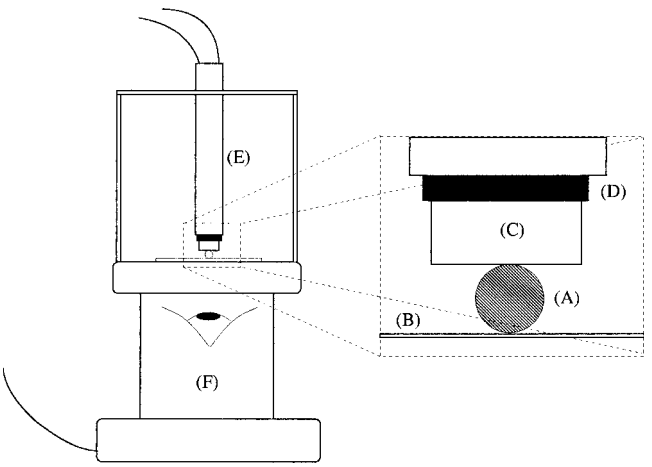

Figure 8 Sketch of the experimental setup: (F) inverted microscope; (E) linear DC actuator and linear strain gauge, (C) movable ''probe'' connected to the actuator (D); (A) spherical particle ~ 100–700 μm in diameter (bead); (B) microscope slide. The drawing is not to scale.

MATERIALS

The gel beads are supplied by VersaMatrix A/S and consist of a crosslinked poly(ethylene glycol) (PEG) network. The beads are synthesized from PEG macromonomers having oxetane rings at each end (see Ref. [3] for further details). The PEG macromonomers range from 400 to 2000 g/mol and the resultant beads are termed according to the size of the macromonomer type used in the synthesis. For example, beads produced from the 400 g/mol macromonomer are termed Versabead O400. A larger PEG macromonomer results in a larger distance between crosslinks in the final network, wherefore the rigidity of the beads generally decreases as the precursor macromonomer increases. This makes it possible to compare experimental and simulated stress–strain data for a range of experimentally obtained moduli.

RESULTS AND DISCUSSION

In this section we present and discuss simulations and experimental measurements. It is noted that all measurements were carried out on beads swollen to their equilibrium in water at ambient temperature (~ 22°C).

In Figure 5(a) a mesh of 3719 triangular elements (7620 velocity nodes and 1951 pressure nodes) can be seen. This is the fine mesh used in our simulations. A coarser mesh with 959 elements (2010 velocity nodes and 526 pressure nodes) is used in some simulations to save simulation time. In all simulations, a time step of $\Delta t = 0.1$ s is used, which was found to be sufficiently small to avoid any appreciable error accumulation. Also an axial displacement velocity of $\dot{h} = -0.1\ \mathrm{s}^{-1}\ R_0$ is used in all simulations, which means that each time step corresponds to a 1% increase in axial displacement. In Figure 5(b) the fine mesh can be seen at a 65% axial displacement.

Before the relationship between E_a and the shear modulus G is investigated, an analysis of how the stress–strain behavior changes while going from purely viscous to purely elastic deformations is performed. Therefore, simulations with varying relative contributions from elastic and viscous forces are carried out. For our geometry, we define a dimensionless number Λ given in eq. (19). This ratio indicates the magnitude of the elastic contribution to the stresses relative to the viscous contribution.

$$\Lambda = \frac{GR_0}{\mu(-\dot{h})} \tag{19}$$

In eq. (19), $\dot{h}$ is the axial displacement velocity as described in earlier section and R_0 is the initial radius of the sphere. When Λ is small, viscous forces dominate relative to the elastic forces and *vice versa*.

By carrying out simulations with Λ increasing from 10^{-6} to 10^{6} in decade steps, the flow regimes given in Table I have been found. These simulations were only carried out for deformations up to 40% because of stability issues, which are discussed below.

As explained in earlier section, stability is gained by splitting $\gamma_{[0]}$ into an explicit and an implicit part; however, problems arise when the flow approaches the elastic limit. When $\Lambda > 10^3$ it is only possible to carry out simulations for small axial displacements. Also, when the Mooney-Rivlin parameter q is increased (from 0) the instability increases. In Figure 9 curves indicating the stability limit for different values of q are drawn. This figure is prepared by carrying out simulations until instability sets in at various values of Λ and q and then plotting the points of instability as a function of Λ. This means that the areas below the curves are stable while the areas above the curves are unstable. The figure shows that it is only possible to carry out close to purely elastic simulations, $\Lambda \sim 10^3$, up to large displacements ($\approx 70\%$) when $q = 0$. Therefore, a compromise between degree of elasticity and degree of deformation has to be made if one needs to carry out simulations with $q > 0$.

In Figure 10 examples of stress–strain curves from each of the flow types can be seen. To compare these curves with each other, the stresses are normalized by the maximum stress in each of the simulations. The curves show that the initial part of the curve is only close to linear in the elastic case while it gets increasingly nonlinear as viscous effects increase. Therefore, the relation between the apparent modulus and shear modulus is only investigated in the elastic limit. This is done by carrying out simulations with all parameters constant except the shear modulus and then making a linear fit to the initial linear part of the curves. The Hertz's expression is also fitted to the corresponding force–displacement data at low displacements to obtain the Hertz's modulus. The Hertz's modulus can be used as a means for checking the finite element model because we assume in the finite element model that the beads are incompressible. The Hertz's modulus is related to the shear modulus by

$$E^* = \frac{E}{1-\nu^2} = \frac{2(1+\nu)}{1-\nu^2} G$$

This means that we expect the Hertz's modulus to be $E^* = 4G$. In Table II apparent moduli found from fits

TABLE I
Type of Flow at Various Values of Λ

Viscous	$\Lambda \in [0; 10^{-3}]$
Viscoelastic	$\Lambda \in [10^{-3}; 10^{3}]$
Elastic	$\Lambda \in [10^{3}; \infty]$

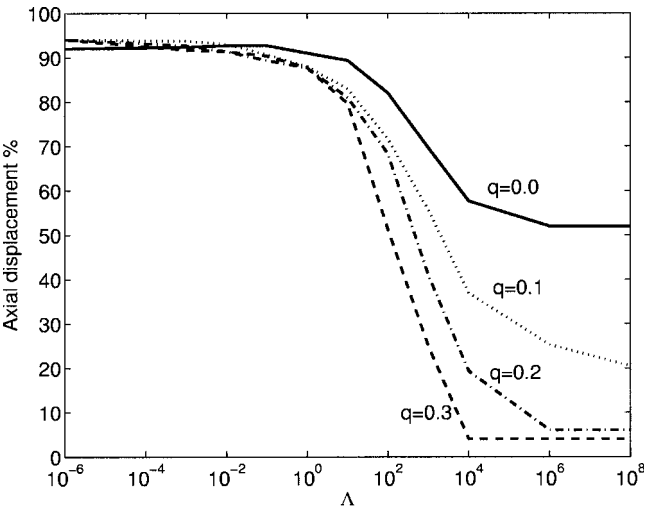

Figure 9 Area of stability for the sphere geometry at various q values. The curves show at which axial displacement instability sets in for various values of Λ. Areas below the curves correspond to stable combinations of axial displacement and Λ. Nine hundred fifty-nine elements, 2010 velocity nodes, and 526 pressure nodes were used in the simulations.

to the initial linear part of simulated stress–strain curves can be seen together with the Hertz's moduli obtained from the corresponding force–displacement curves.

The results presented in Table II indicate that the apparent modulus indeed is related to the shear modulus because it scales with the shear modulus approximately as $E_a \sim 4G$. Also the Hertz's moduli obtained from the stress–strain curves agree very well with the expected relationship for incompressible materials, namely that $E^* = 4G$. The good agreement obtained for the Hertz's modulus indicates that

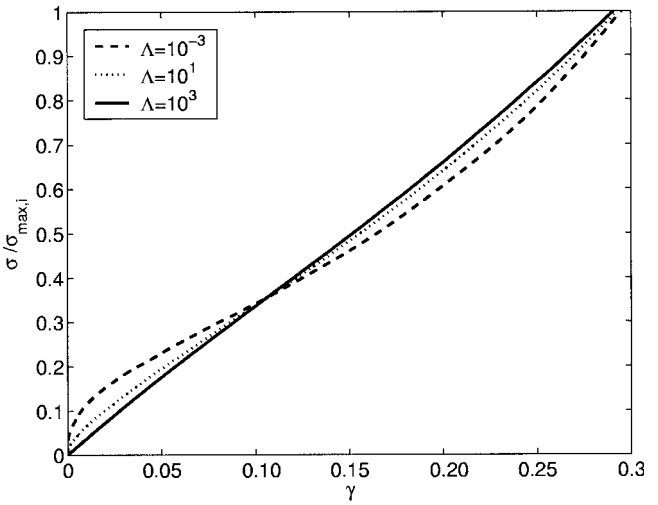

Figure 10 Simulated stress–strain curves for different values of Λ. For each curve the stresses are normalized by the maximum stress from each simulation ($\sigma_{max,i}$).

TABLE II
Ratio between the Apparent Modulus Found from Linear Fit to Simulated Stress–Strain Data and the Shear Modulus (E_a/G)

G (Pa)	Λ	E_a/G	E^*/G
10^2	10^3	3.93	4.20
10^3	10^4	3.89	4.01
10^4	10^5	3.88	4.00
10^5	10^6	3.88	4.00

Simulations are carried out for various values of the shear modulus G while keeping the viscosity constant at $\mu = 1$ Pa s. Also shown is E^*/G. The fine mesh was used in the simulations (3719 elements) and E_a was found by a linear least square fit for $\gamma \in [0; 0.15]$. The Hertz's modulus E^* was found by fitting equation 1 to the force–displacement data for $h/D_0 \in [1; 0.9]$, i.e. below 10% displacement.

our model in fact gives the correct force–displacement behavior at least for small displacements ($\leq$10%). If $E_a \sim 4G$ it should be possible to simulate stress–strain curves that agree with experimentally obtained curves by determining E_a from the experimental data and then using $G = E_a/4$ as the input to the model. This, of course, implies that the beads behave as purely elastic bodies. In Figure 11 experimentally obtained stress–strain data for a Versabead O1000 are shown together with two simulations and a linear fit to the initial part of the experimental data points. The linear fit leads to $E_a = 4.89$ MPa and therefore $G = 4.89$ MPa/4 = 1.22 MPa is used as input to the model. The simulation with the Mooney-Rivlin parameter being $q = 0$ shows a nice agreement with the experimental data points at low strains ($\gamma < 0.2$). However, as the strain increases so does the deviation between the simulated curve and the experimental curve. This indicates that the beads show some degree of strain hardening and therefore simulations with various q parameters are carried out. By trial and error, $q = 0.25$ is found to give a nice fit between experimental data and simulated data. However, at large deformations it is not possible to carry out purely elastic simulations for $q = 0.25$ due to instability (a strain $\gamma = 0.5$ corresponds to an axial displacement of 69%). Therefore, the simulations shown in Figure 11 were carried out with $\Lambda = 50$, i.e., viscous contribution is not negligible. Nevertheless the simulated curve with $q = 0.25$ gives a nice fit to the experimental data, indicating that the apparent modulus is a real modulus.

In Figure 12, experimental stress–strain data for different types of beads can be seen together with simulated curves. The shear moduli used in the simulations are estimated from the apparent moduli found from the experimental data. In Table III parameters used in the simulations are listed. From Figure 12 it is seen that the simulated curves agree well with experimental data except for the Versabead O400. In this case it was necessary to have a very low Λ because of the high q-value needed. The O400 simulated curve shows how the viscous contributions dominate at low strains resulting in an ''overshoot'' of the stresses compared with the experimental data. The results in Figure 12 and Table III indicate that the real beads behave as elastic bodies because it is necessary to have a high Λ value to get good agreement between simulated and experimental curves at low strains. Comparison of the q-values necessary to obtain satisfactory agreement between experimental and simulated data indicates

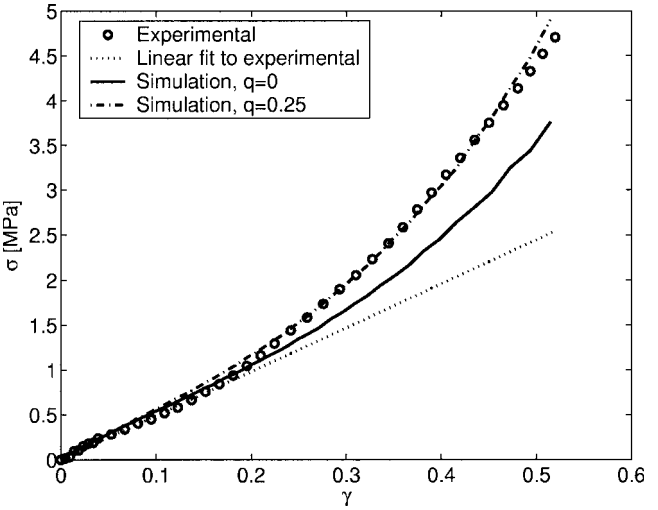

Figure 11 Comparison between experimentally obtained stress–strain data from a Versabead O1000 and simulated data. The linear fit to the experimental data points for $\gamma < 0.15$ leads to $E_a = 4.89$ MPa. $G = E_a/4$ was used as the input to the model. The radius of the bead was $R_0 = 131$ μm. $\Lambda = 50$ was used in the simulations.

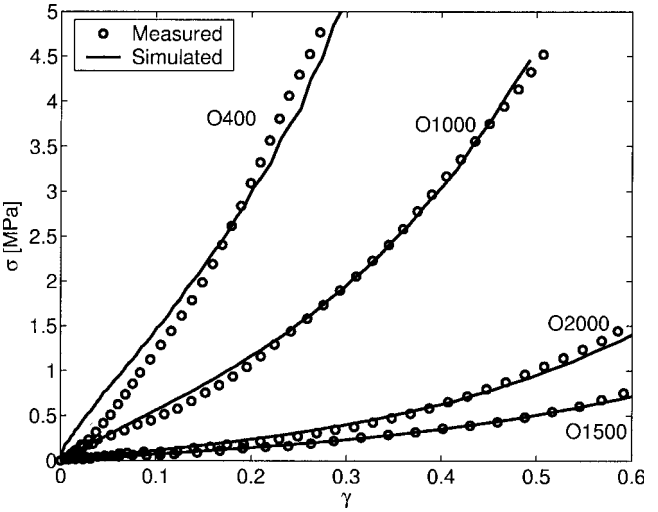

Figure 12 Comparison between experimentally obtained stress–strain data and simulated data. The parameters used in the simulations can be seen in Table III.

TABLE III
Parameters used in the Simulated Curves Shown in Figure 12

Bead type	q	G (MPa)	μ (MPa s)	R_0 (μm)	Λ
O400	0.4	2.14	2.14	133	10
O1000	0.25	1.22	0.24	131	50
O1500	0.05	0.18	0.018	149	100
O2000	0.25	0.25	0.05	155	50

The viscosity is adjusted to obtain sufficient stability while the shear modulus is estimated from the apparent moduli found from the experimental data in Figure 12 (i.e. $G = E_a/4$).

that strain hardening effects increase with increasing elastic modulus.

Because the pressure enters the calculation of the axial compression force, it is interesting to investigate how the pressure distribution differs for simulations carried out with different values of q. In Figure 13 the pressure distribution for a simulation with $\Lambda = 100$ can be seen at 65% displacement. In Figure 13(a) $q = 0$ and it is seen that the largest pressure is concentrated around the center of the contact interface. In Figure 13(b) the pressure distribution can be seen for a simulation with $q = 0.2$. Again the largest pressures are in the center of the contact interface. However, when Figures 13(a and b) are compared it is seen that the pressures are higher at the contact interface in Figure 13(b) and that the pressure gradient is considerably larger in the latter case. This indicates that the strain hardening effects result in an increase in the pressure at the contact interface and thereby increasing the compression forces.

CONCLUSIONS

A viscoelastic finite element model has been set up and solved to investigate the compression of spherical polymer gel beads. The finite element method used is stable for flows ranging from purely viscous to close to purely elastic. However, the stability of the method decreases for increasing values of the Mooney-Rivlin parameter q. This means that simulations carried out using $q \gtrsim 0.4$ require a viscous contribution to the stress that is unrealistic compared to the elasticity of the beads to avoid instability.

Using simulated results at low strains ($\gamma < 0.15$) it has been found that an apparent modulus E_a can be extracted from data obtained from a mechanical test where the compression force and the central lateral expansion are measured. The simulations indicate that the apparent modulus is related to the shear modulus approximately as $E_a \sim 4G$; however, the method can only be used for elastic deformations. If viscous effects are prominent the stress–strain curves are nonlinear at small strains and thus the modulus cannot easily be extracted. Comparison between stress–strain curves obtained from real measurements and simulations indicate that the beads behave as elastic bodies with some degree of strain hardening. As long as the strain hardening effects are low, it is possible to simulate stress–strain curves that agree well with real measurements, indicating that the apparent modulus is a real measure of the elastic modulus. The pressure distribution inside the bead depends strongly on the Mooney-Rivlin parameter q. Example simulations with $q = 0$ and $q = 0.2$ show that the pressure gradient in the axial direction is much larger in the latter case and that the pressure is higher at the contact interface when $q = 0.2$

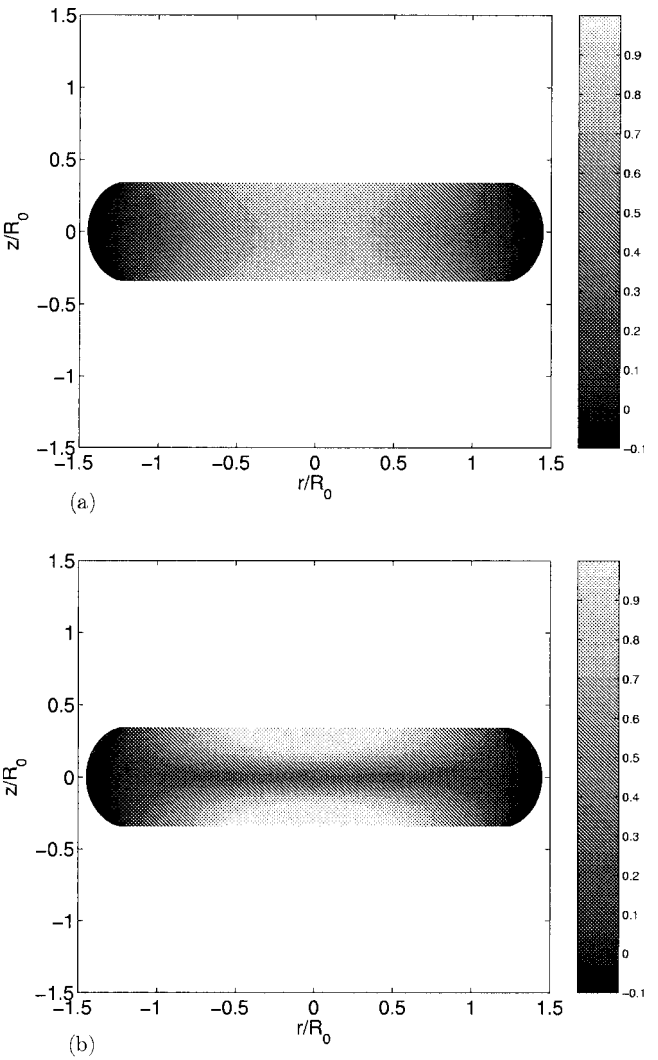

Figure 13 Pressure distribution inside the bead at 65% displacement. The pressure scale is relative to the maximum pressure for the simulation with $q = 0.2$ (The maximum pressure is in the center of the contact interface, i.e., $r = 0$ and $z = h$.) The parameters used were $G = 10^5$ Pa and $\mu = 10^4$ Pa s ($\Lambda = 100$). (a) Pressure distribution when $q = 0$; (b) pressure distribution when $q = 0.2$. The fine mesh was used in the simulations.

compared to $q = 0$. This means that the increase in compression force observed for increasing q-value can partly be explained by an increase in the pressure at the contact interface.

References

1. Landau, L. D.; Lifshitz, E. M. Course of Theoretical Physics. 7: Theory of Elasticity, 2nd ed.; Pergamon: Elmsford, NY, 1970.
2. Treloar, L. R. G. Proc R Soc London Ser A 1976, 351, 301.
3. Grøtli, M.; Rademann, J.; Groth, T.; Lubell, W.; Miranda, L. P.; Meldal, M. J Comb Chem 2001, 3, 28.
4. Rademann, J.; Grøtli, M.; Meldal, M.; Bock, K. J Am Chem Soc 1999, 121, 5459.
5. Andrei, D. C.; Briscoe, B. J.; Luckham, P. F.; Williams, D. R. J de Chimie Physique et de Physico-Chimie Biologique 1996, 93, 960.
6. Knaebel, A.; Rebre, S. R.; Lequex, F. Polym Gels Networks 1997, 5, 107.
7. Liu, K. K.; Williams, D. R.; Briscoe, B. J. J Phys D: Appl Phys 1998, 31, 294.
8. Hertz, H. J für die Reine und Angewandte Math 1882, 92, 156.
9. Tatara, Y. J Eng Mater Technol 1991, 113, 285.
10. Harlen, O. G.; Rallison, J. M.; Szabo, P. J Non-Newtonian Fluid Mech 1995, 60, 81.
11. Rasmussen, H. K. J Non-Newtonian Fluid Mech 2000, 92, 227.
12. Rasmussen, H. K. J Non-Newtonian Fluid Mech 2002, 106, 107.
13. Bird, R. B.; Armstrong, R. C.; Hassager, O. Dynamics of Polymeric Liquids, Vol. 1; Wiley: New York, 1987.
14. Bird, R. B.; Armstrong, R. C.; Hassager, O.; Curtiss, C. F. Dynamics of Polymeric Liquids, Vol. 2; Wiley: New York, 1987.
15. Zienkiewicz, O. C.; Tayler, R. L. The Finite Element Method, 4th ed.; McGraw-Hill: New York, 1994; Vol. 1.
16. Rasmussen, H. K.; Hassager, O. J Non-Newtonian Fluid Mech 1993, 46, 298.